Electro-Thermal Homogenization of HTS Stacks and Roebel Cables for Machine Applications

Casper Leonard Klop, Runar Mellerud, Christian Hartmann and Jonas Kristiansen Nøland

***Abstract*—This paper presents a homogenized electro-thermal model for high-temperature superconductor (HTS) stacks made of multiple REBCO tapes, which reduces the computational complexity of their thermal analysis. The electromagnetic analysis is performed in both the *H*- and *T*–*A*-formulation. An average heat capacity and an orthotropic heat conductivity are derived for the equivalent thermal properties of the HTS coil. The proposed homogenization method is verified to produce the same results as the full model with an error below 5% for a range of scenarios, including transport losses, magnetization losses, AC frequencies from 50 to 300 Hz and a temperature range from 25 to 80 K. Finally, the model is applied to study a permanent magnet motor with HTS armature windings and is verified to produce results with an error below 15 % as long as the stabilizer eddy current losses are low. Compared to the full multilayer model, the newly proposed model allows for the use of a significantly coarser mesh, which reduces the computation time by an order of magnitude.**

***Index Terms*—H-formulation, Numerical Modeling, HTS, REBCO, TA-formulation, Thermal Analysis.**

I. Introduction

THE steady decrease in the cost of high-temperature superconductors (HTS) has recently led to an increased interest in their large-scale applications. One of the most commonly used HTS materials is REBCO, which is produced in thin tapes. In some of its potential applications, such as electrical machines, fault limiters and high-field magnets, the HTS tapes are subject to AC conditions.

When HTS tapes carry AC currents or experience alternating magnetic fields, they are subject to AC losses, which generate heat. The resulting rise in temperature deteriorates the superconducting properties of the HTS tapes, creating a positive feedback loop. Therefore, a coupled electro-thermal model of the HTS stack is needed to determine the required cooling capacity and the resulting equilibrium temperature. Thus far, analysis of the electro-thermal behavior of HTS conductors has been limited to single tapes or small stacks, with models that include the REBCO layer, the stabilizer, the substrate, and the insulation materials [1–3].

Nevertheless, scaling up the electromagnetic analysis from HTS tapes to coils presents a significant challenge due to the high computational complexity associated with the high aspect ratio of HTS tapes. *Homogenization* is a commonly used approach to mitigate this issue. In this approach, the different layers of the HTS coil are represented by a single material with equivalent electromagnetic properties [4, 5]. Ideally, this homogenization method can be applied in electro-thermal analyses as well. Two previous papers proposed steps towards a homogenized thermal model: Firstly, Hu *et al.* (2017) present such a model for a single HTS tape [6], but their model is not directly applicable to a coil due to its anisotropic nature. Secondly, Tomków *et al.* (2020) proposed an anisotropic coil model, but did not couple this to an electromagnetic model [7].

To address the above-mentioned problem, a homogenized electro-thermal model of an HTS coil has been proposed by deriving its equivalent thermal properties and coupling the thermal analysis to the homogenized electromagnetic analysis, performed in the *H*-formulation [8]. This paper expands upon the previous work by replacing the *H*-formulation with the *T*–*A*-formulation, and by applying the new method to the analysis of the armature windings of an electrical machine, which consists of HTS Roebel cables.

The *T*–*A*-formulation is known to be faster than the *H*-formulation [5] and has been successfully used to analyze superconducting machines [9]. This study will determine whether electro-thermal homogenization of HTS coils can be further sped up by using the homogenized *T*–*A*-formulation. The aim is to simplify and speed up the electro-thermal analysis of HTS coils using finite element analysis (FEA) across various scenarios, including:

1) AC currents at 50 & $300\,\mathrm{Hz}$;
2) External AC magnetic fields; and,
3) Submerged in liquid nitrogen (LN_2) & hydrogen (LH_2).

Afterward, the homogenization method is applied to the analysis of a superconducting aircraft motor to demonstrate its applicability.

This paper is structured as follows: first, Section II outlines the proposed method and the relevant material properties. Then, Section III compares the original and homogenized models for several simple cases, after which the homogenized coil model is implemented in the analysis of an electrical machine in Section IV. Section V evaluates the accuracy and applicability of electro-thermal homogenization, and finally, Section VI concludes the paper and highlights future work.

II. Methodology and Assumptions

The electromagnetic analysis in this study is performed using the *H*-formulation [10] and the homogenized *T*–*A*-formulation [11], which are coupled to a heat transfer module in an FEA environment. The coupling between the two modules is bidirectional: losses calculated by the electromagnetic

Manuscript received XXXXXX, 20XX; revised XXXXXXX, 20XX; accepted XXXXXXXXXX, 20XX. Date of publication XXXXXXXXXX, 20XX. (*Corresponding author: Casper Leonard Klop.)*

C.L. Klop, R. Mellerud, C. Hartmann and J.K. Nøland are with the Department of Electric Energy, Norwegian University of Science and Technology (NTNU), Trondheim, 7491 Norway. C. Hartmann is with the Institute for Energy Technology, Halden, Norway, as well.

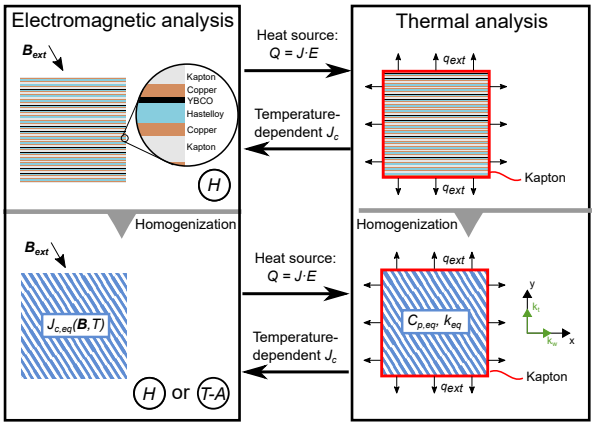

Fig. 1. Illustrative overview of the proposed method presented in this paper.

analysis are implemented as a heat source, and the calculated temperature distribution influences the local critical current density of the HTS tapes. Fig. 1 provides an overview of the method proposed in this paper.

The proposed method is verified by analyzing a coil with 20 turns surrounded by a cryogenic fluid. The detailed dimensions of the coil are provided in Table I. Each tape is wrapped in Kapton insulation, and the silver overlayer is neglected as it behaves similarly to copper at cryogenic temperatures. The homogenized *T–A* model is compared to the 'full' *H* model, which includes every individual material and is used as a baseline.

A. Electromagnetic Model

In the previous work, the electromagnetic analysis for both the 'full' and the homogenized model was performed using the *H*-formulation [8]. In this work, the homogenized *T–A*-formulation [11] is used and compared to the earlier results.

In the *T–A*-formulation, the current vector potential, defined by $\mathbf{J} = \nabla \times \mathbf{T}$, is used in the superconducting region. This is superimposed on the magnetic vector potential ($\mathbf{A}$) formulation, which is used in the non-superconducting regions as well. The governing equations are given by eqs. (1) and (2), respectively.

$$\nabla \times \left(\frac{1}{\sigma} \nabla \times \mathbf{T} \right) = -\frac{\partial \mathbf{B}}{\partial t} \tag{1}$$

$$\nabla^2 \mathbf{A} = -\mu \mathbf{J} \tag{2}$$

Furthermore, it is assumed that the thickness of the superconducting layers can be neglected. This means that the influence of the parallel magnetic field is neglected, and that the current density is simply given by $J_z = \partial T_y / \partial x$.

In eq. (1), the permeability μ of each material is assumed to be equal to μ_0, and the electrical conductivity σ of the non-superconducting materials is given in Table I. The resistivity of copper, with an assumed residual resistance ratio (RRR) of 50, varies with temperature [12].

TABLE I
COIL AND MATERIAL PARAMETERS

Description	Symbol	Value
Number of turns	n_t	20
Tape width	w_t	4 mm
REBCO thickness	h_{HTS}	1 μm
Copper thickness	h_{Cu}	20 μm
Hastelloy thickness	h_{sub}	50 μm
Kapton thickness	h_{ins}	60 μm
YBCO density	ρ_{YBCO}	5900 kg/m^3
Copper density	ρ_{Cu}	8000 kg/m^3
Hastelloy density	ρ_{sub}	8280 kg/m^3
Kapton density	ρ_{ins}	1420 kg/m^3
Copper electrical conductivity	σ_{Cu}	See [12]
Hastelloy electrical conductivity	σ_{sub}	3.33×10^6 S/m
Kapton electrical conductivity	σ_{ins}	1×10^{-3} S/m [a]

[a] Higher than the physical value for numerical stability improvement

The resistivity of REBCO is commonly described by a relation known as the *E-J* power law, given by:

$$E = E_0 \left(\frac{J}{J_c(B,T)} \right)^n, \tag{3}$$

where $E_0 = 10^{-4}\ V/m$. This model uses the material properties of a REBCO HTS tape from Shanghai Superconductor, which are available in the Robinson HTS Database [13]. Although exponent n varies with both B and T in reality, a fixed value of 28 is chosen for simplicity.

The critical current density J_c is a function of both the external magnetic field $\mathbf{B}$ and the temperature T. The field-dependency is modeled using an anisotropic Kim-like model [14, 15], as shown in eq. (4). The relevant parameters are fitted to the experimental data and given in Table II.

$$J_c(\mathbf{B},T) = J_{c0} \cdot \underbrace{\left(1 + \frac{\sqrt{(kB_\parallel)^2 + B_\perp^2}}{B_0} \right)^{-\alpha}}_{\text{Kim-like model}} \cdot \underbrace{\gamma(B,T)}_{\substack{\text{Temperature} \\ \text{dependence}}} \tag{4}$$

The temperature dependency $\gamma(B,T)$, given in eq. (5), is approximately independent of the magnetic field for temperatures below 77 K. In this case, the temperature dependency is modeled using an exponential equation normalized around 35 K [16]. For cooling with liquid nitrogen (LN_2), the operating temperatures start approaching the critical temperature of REBCO, which is influenced by the magnetic field. In this case, a linear approximation is fitted to the experimental dataset provided in [13], which decreases from the critical current at 77 K to zero at the critical temperature $T_c(|B|)$.

$$\gamma(B,T) = \begin{cases} e^{\frac{-(T-T_{ref})}{T^*}} & 20\,\text{K} < T < 77\,\text{K} \\ \frac{T_c(|B|)-T}{T_c(|B|)-77\,\text{K}} & 77\,\text{K} < T < T_c(|B|) \\ 0 & T > T_c(|B|) \end{cases} \tag{5}$$

Currents are applied by setting the correct boundary conditions. These are either integral constraints in the *H*-formulation [17], or Dirichlet and Neumann boundary conditions in the *T–A*-formulation [11].

TABLE II
CRITICAL CURRENT DENSITY PARAMETERS

Description	Symbol	Value
J_c at 0 T, 35 K	J_{c0}	2.88×10^{11} A/m^2
Critical current at 0 T, 35 K	I_0	1152 A per tape
J_c at 0 T, 77 K	J_{c0}	6.77×10^{10} A/m^2
Critical current at 0 T, 77 K	I_0	271 A per tape
E-J law exponent	n	28
Kim model parameter	k	0.25
Kim model parameter	B_0	0.03 T
Kim model parameter	α	0.6
Reference temperature	T_{ref}	35 K
Temperature fit	T^*	32 K

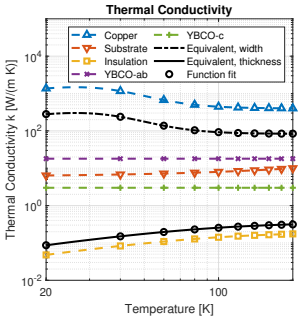

Fig. 2. Thermal conductivity of the individual materials and the equivalent values.

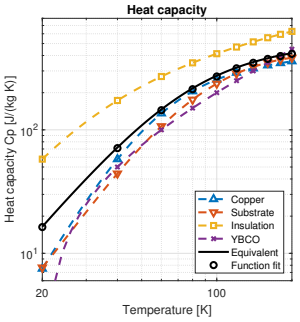

Fig. 3. Specific heat capacity of the individual materials and the equivalent values.

B. Thermal Model

The governing equation of the thermal model is given in eq. (6).

$$\rho C_p \frac{\partial T}{\partial t} - \nabla \cdot (k \Delta T) = Q + q_{ext} \tag{6}$$

For each material, the mass density ρ, the specific heat capacity C_p and the thermal conductivity k are required. The mass density is provided in Table I, and the latter two parameters are shown in Figs. 2 and 3. The heat capacity and thermal conductivity of copper (RRR=50) and Kapton have been acquired from the NIST database [18]. This database provides temperature-dependent parameters as functions with fitted coefficients. For Hastelloy, the thermal properties are based on the data provided in [19], to which the same equation used in the NIST database is fitted. The thermal properties of REBCO are based on [3]. REBCO has a different in-plane (*ab*) and out-of-plane (*c*) thermal conductivity.

The internal heat generation is given by $Q = J \cdot E$, calculated by the *H*- or *T*–*A*-formulation, and q_{ext} represents the convective heat flow to the exterior. The thermal boundary condition of eq. (6) is defined by a fixed convective heat transfer coefficient of $h = 400\,\mathrm{W/(m^2K)}$ using the following equation:

$$q_{ext} = hA(T_{surf} - T_{ext}) \tag{7}$$

The initial temperature of the coil is assumed to be equal to that of the surrounding medium, which is 25 K for liquid hydrogen (LH_2), and 77 K for liquid nitrogen (LN_2).

C. Homogenization Approach

Homogenization of the electromagnetic analysis based on the *H*-formulation was initially described in [4]. This method neglects the non-superconducting materials and calculates an equivalent critical current density $J_{c,eq}$ based on the volume fraction of the superconducting layer. Even though the resulting current density and losses are 'smeared out' over the surface area, the model is still able to reproduce the AC losses accurately while being an order of magnitude faster than the full model, which takes into account all layers.

Homogenization of the *T*–*A*-formulation is performed in a similar way [11]. An equivalent current density is derived, and the losses are distributed over a 2D region with equivalent properties. Even though the *T*–*A*-formulation is now defined on a 2D region, the influence of the parallel magnetic field is still neglected.

This study proposes a similar approach for the thermal analysis, by replacing the different layers with a homogeneous material. The homogenized thermal analysis can then be coupled to the homogenized electromagnetic model. Due to the low thermal conductivity of Hastelloy and especially Kapton relative to that of copper, nearly all heat flow is parallel to the width of the HTS tapes, referred to as the x-direction in Fig. 1. Therefore, an orthotropic heat conductivity is derived for the equivalent thermal properties of the HTS coil. For the conductivity in the x-direction, along the width of the HTS tape, the thermal resistance of each material is considered in parallel:

$$R_{eq,w} = \frac{1}{\sum_1^n \frac{1}{R_n}} \;\rightarrow\; k_{eq,w} = \frac{\sum_1^n k_n t_n}{\sum_1^n t_n}, \tag{8}$$

where k_n and t_n represent the thermal conductivity and the thickness of the n^{th} layer, respectively. Similarly, the thermal conductivity in the y-direction is given by considering the thermal resistances in series:

$$R_{eq,t} = \sum_1^n R_n \;\rightarrow\; k_{eq,t} = \frac{\sum_1^n t_n}{\sum_1^n \frac{t_n}{k_n}}. \tag{9}$$

With low-conductivity Kapton in between every tape, $k_{eq,t}$ will be close to the thermal conductivity of Kapton, and will thus be relatively low compared to $k_{eq,w}$. Finally, the equivalent specific heat capacity is equal to the mass-based average of the heat capacity of each material:

$$C_{p,eq} = \frac{\sum_1^n C_{pn} m_n}{\sum_1^n m_n} = \frac{\sum_1^n C_{pn} \rho_n t_n}{\sum_1^n \rho_n t_n}. \tag{10}$$

The temperature-dependent thermal properties are given in Figs. 2 and 3. A function of the same form as those provided by the NIST database is fitted to each equivalent property, and provided in the Appendix.

D. Finite Element Analysis Implementation

Finite Element Analysis (FEA) of the HTS coil is performed in COMSOL Multiphysics, and simulated on a Dell PowerEdge C6520 node of a high-performance cluster [20]. The implementation of the electromagnetic analysis is based on the original and homogenized models described in [4, 11].

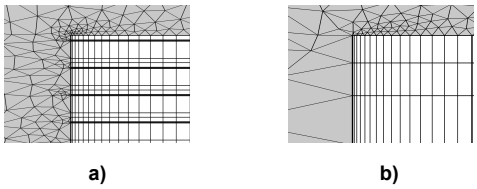

Fig. 4. Mesh refinement for the a) full model and b) homogenized model. At the outer 10% of the tape, the mesh is finer than in the middle.

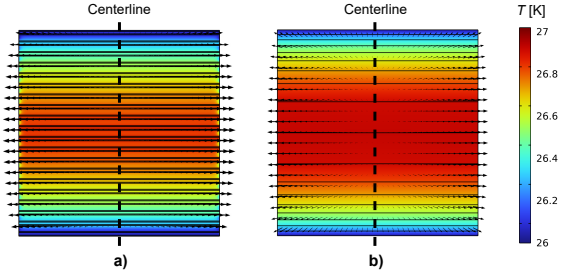

Fig. 5. Examples of temperature maps (Case 1, t = 0.177 s) for the a) full and b) homogenized model. The arrows represent the conductive heat flux.

The thermal model is defined on the HTS coil, and the cryogenic medium around it is assumed to have a constant temperature. The orthotropic thermal conductivity of the homogenized model is implemented as a diagonal conductivity matrix, with $k_{11} \neq k_{22}$.

The outer insulation layer is modeled as a one-dimensional *thin layer*, defined at the outer boundary (shown in red in Fig. 1). This assumes all heat flow is perpendicular to the boundary, and provides a more robust mesh. On this same boundary, a convective boundary condition is defined as described by eq. (7).

A rectangular structured mesh is used in the coil, and a mesh refinement study showed that 80 nodes along the width provided sufficient accuracy. The outer edges of the tapes have a finer mesh, shown in Fig. 4, because the current density and magnetic field experience strong gradients here. The HTS formulations and the thermal module use a linear discretization, while the *A*-formulation uses quadratic discretization. A relative tolerance of 5×10^{-5} has been used for all models.

The homogenization method outlined in this paper is applied to four test cases, shown in Table III, each of which is run for 10 electric cycles of the fundamental frequency. The cases are selected to demonstrate the different effects of the electrical frequency, the temperature, and the loss distribution of transport losses versus magnetization losses. An example of the obtained results is shown in Fig. 5.

TABLE III
OVERVIEW OF CASES

Case	Temperature	Current	Magnetic flux density
1	25 K	200 A, 50 Hz	None
2	25 K	150 A, DC	150 mT, 50 Hz
3	25 K	200 A, 300 Hz	None
4	77 K	90 A, 50 Hz	None

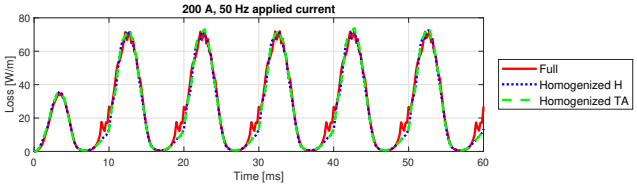

Fig. 6. The electromagnetic losses in the full and homogenized models for an applied current of 200 A at 50 Hz.

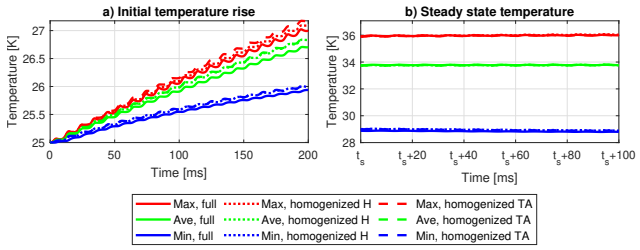

Fig. 7. The a) initial temperature rise and b) steady-state temperature for the full and homogenized models for an applied current of 200 A at 50 Hz.

III. RESULTS

A. Case 1: AC Current

In the first case, a 200 A AC current ($0.17 I_0$) at 50 Hz is applied to each tape. The homogenized model reproduces the simulated magnetic field and electric current distribution of the full model well, as has been reported in [4]. Fig. 6 shows the resulting transport losses for both models. The results from the homogenized *H*-formulation, described in [8], are shown as well for comparison.

Fig. 7a shows the initial temperature rise. The homogenized model overestimates the average temperature rise after 10 cycles by 0.1 K. However, Fig. 7b shows all models reach the same steady-state temperature distribution after time t_s.

The coil does not heat up uniformly, but becomes warmer in the center, further away from the cryogenic medium. The homogenized model captures this effect, as shown in Fig. 8. In this graph, the temperature is plotted along the centerline shown in Fig. 5. Fig. 9 shows that the homogenized model predicts a marginally higher external heat flow, which is caused by the overestimation of the temperature rise.

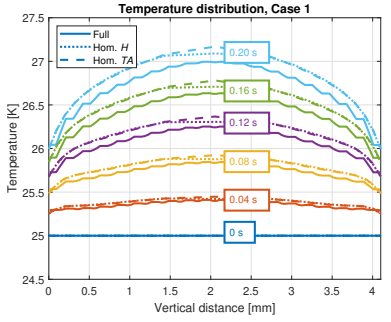

Fig. 8. The temperature along a vertical cutline in the center of the coil for Case 1.

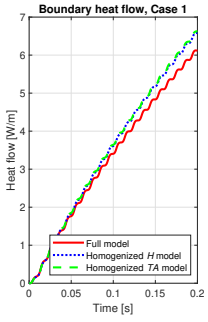

Fig. 9. The external heat flow for Case 1.

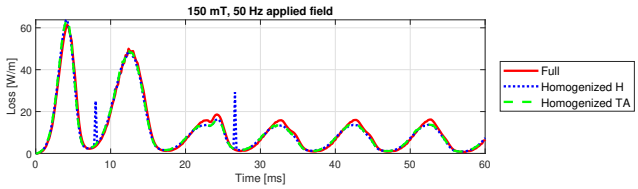

Fig. 10. The electromagnetic losses in the full and homogenized models for an applied field of 150 mT at 50 Hz.

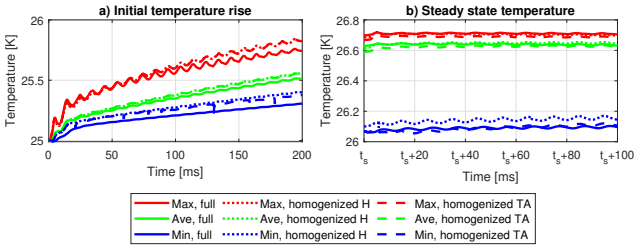

Fig. 11. The a) initial temperature rise and b) steady-state temperature for the full and homogenized models for an applied field of 150 mT at 50 Hz.

B. Case 2: AC Field

In the second case, a perpendicular external magnetic field of $150\,\mathrm{mT}$ at $50\,\mathrm{Hz}$ is applied, while each tape carries a DC current of $150\,\mathrm{A}$ ($0.13I_0$). For this, a Dirichlet boundary condition, as described by eq. (11), is added to the outer boundaries of the model. $\vec{H}_{encl}$ refers to the magnetic field generated by the enclosed current and is approximated by treating the coil as a point source.

$$\vec{H}_{boundary} = \vec{H}_{ext} + \vec{H}_{encl} \tag{11}$$

Figs. 10 and 11 show the magnetization losses and associated temperature loss. The maximum and average steady-state temperatures are predicted accurately, though the temperature rise of the homogenized model is less accurate than in Case 1. Fig. 12 shows that most of the temperature increase occurs at the top and bottom of the coil. This is because the losses caused by the perpendicular magnetic field concentrate here. The homogenized model captures this effect, but overestimates the average temperature rise by $0.05\,\mathrm{K}$ after 10 cycles.

C. Case 3: Higher Electrical Frequency

The electrical frequency is known to have a significant effect on the magnitude and the distribution of the losses in HTS tapes and coils [21]. To determine whether the homogenized model captures this effect at higher frequencies, a $200\,\mathrm{A}$ AC current at $300\,\mathrm{Hz}$ is applied.

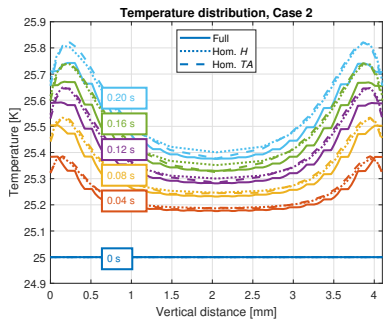

Fig. 12. The temperature along a vertical cutline in the center of the coil for Case 2.

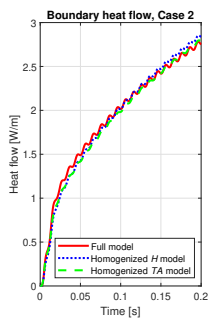

Fig. 13. The external heat flow for Case 2.

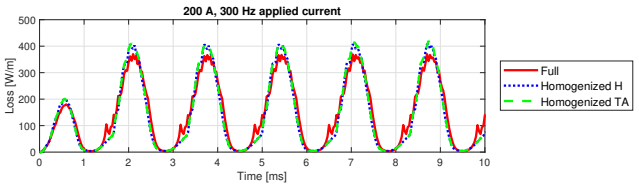

Fig. 14. The electromagnetic losses in the full and homogenized models for an applied current of 200 A at 300 Hz.

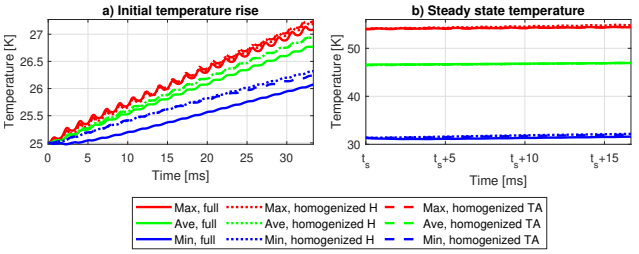

Fig. 15. The a) initial temperature rise and b) steady-state temperature for the full and homogenized models for an applied current of 200 A at 300 Hz.

Figs. 14 and 15 show that the homogenized model reproduces the results with an error below $10\,\%$, except for the minimum coil temperature. Further analysis revealed that this minimum temperature in the full model is located in the Kapton layer, and that the temperature distribution of the REBCO layers is reproduced correctly. Furthermore, integrating the losses gives approximately the same loss per cycle as in Case 1, which is consistent with the finding that the AC transport current losses are proportional to the electrical frequency [21].

D. Case 4: LN_2 Temperature

To analyze the performance of the model in an LN_2 temperature range, an AC current of $90\,\mathrm{A}$ ($0.33I_0$) at $50\,\mathrm{Hz}$ is

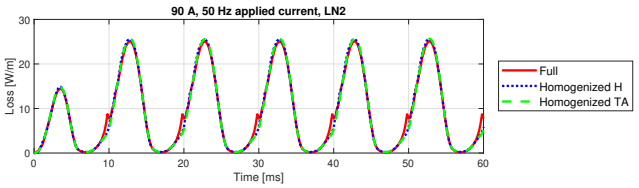

Fig. 16. The electromagnetic losses in the full and homogenized models for an applied current of 90 A at 50 Hz in LN_2.

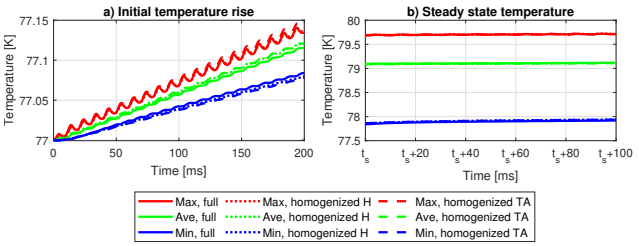

Fig. 17. The a) initial temperature rise and b) steady-state temperature for the full and homogenized models for a current of 90 A at 50 Hz in LN_2.

applied. Figs. 16 and 17 show that the homogenized model has a higher accuracy than in the previous cases and reproduces the temperature rise with an error below $5\,\%$. It is also observed that the temperature rise of the coil is significantly slower than in the previous cases. This is explained by the fact that the equivalent heat capacity at $77\,\mathrm{K}$ is an order of magnitude larger than at $25\,\mathrm{K}$.

IV. Application Case

To demonstrate the applicability of the newly developed method, it is used to analyse the armature windings of a permanent magnet machine designed for a cryo-electric aircraft. The machine parameters are given in Table IV, and the detailed design is given in [22]. The existing electromagnetic numerical model is extended to include the thermal analysis of the coils.

The machine employs HTS Roebel cables [23] in the armature winding. The individual strands of this cable are not insulated from each other, so new equivalent thermal properties of the cable were derived, given in Figs. 18 and 19. Due to the lack of Kapton layers, the thermal conductivity in the perpendicular direction is not as small as before, but it is still significantly smaller than that in the parallel direction.

Compared to the numerical model presented in [22], the following simplifications are made to speed up the analysis:

1) Saturation of the iron stator core is neglected, and a constant relative permeability of $\mu_r = 2000$ is assumed;
2) The slots are assumed to be flooded with a cryogenic fluid at $40\,\mathrm{K}$ with a convective heat transfer coefficient of $h = 1000\,\mathrm{W}/(\mathrm{m}^2\mathrm{K})$;
3) The machine is simulated while operating at $80\,\%$ of its nominal power.

A. Modeling Approach

The numerical machine model uses a static representation of the Halbach PM rotor to perform a dynamic analysis of the stator [24]. The thermal analysis is implemented similarly to what was described in Section II, while ensuring that the orthotropic material properties are implemented with respect to a rotated coordinate system aligned with the coil orientation.

In the model, half of the HTS coil in one slot is modeled in detail using the full *H*-, homogenized *H*- or homogenized *T*–*A* formulation. The remaining part of the machine is analyzed using the vector potential (**A**) formulation, with the remaining coils modeled as perfect conductors. The interface between the *H*- and *A*- formulations is defined as described in [17]. An illustrated explanation of the approach is shown in Fig. 20.

The Roebel cable is modeled as two stacks of HTS tapes with solder in between them [23]. For the solder, a thermal conductivity of $20\,\mathrm{W}/(\mathrm{m\ K})$ is used [25].

TABLE IV
Machine Parameters (from [22])

Description	Symbol	Value
Nominal power	P	$2.5\,\mathrm{MW}$
Rotational speed	n	$5000\,\mathrm{rpm}$
Electrical frequency	f_{el}	$333\,\mathrm{Hz}$
Phase voltage	U_{ph}	$421\,\mathrm{V}$
Phase current	I_{ph}	$683\,\mathrm{A}$
Number of slots	N_s	24
Number of pole pairs	p	4
Air gap diameter	D_g	$260\,\mathrm{mm}$
Active length	L	$240\,\mathrm{mm}$
Slot width	w_s	$20\,\mathrm{mm}$
Number of turns	N_t	14
Strands per turn	$N_{strands}$	18
HTS strand width	w_{strand}	$1.9\,\mathrm{mm}$
Central gap width	w_{gap}	$0.2\,\mathrm{mm}$

B. Results

The AC losses and the resulting temperature development of the analyzed half of the coil are shown in Fig. 21 and Fig. 22, respectively. The discrepancy between the AC losses of the homogenized models and the full model is $12.9\,\%$. This is larger than in the simple cases, and closer analysis revealed that the difference is caused by neglecting the copper losses. The strong, high-frequency magnetic fields that the coils experience in the machine lead to eddy current losses in the copper, which are shown in Fig. 21 as well. These losses are not accounted for in the homogenized models, leading to an underestimation of the average temperature rise of just below $15\,\%$.

In the analyzed case, the copper losses are approximately $10\,\%$ of the total AC losses, so their effect is limited. This observation motivated the simulation of an additional case in

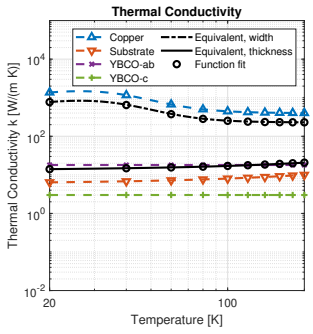

Fig. 18. Thermal conductivity of the individual materials and the equivalent values of the Roebel cable.

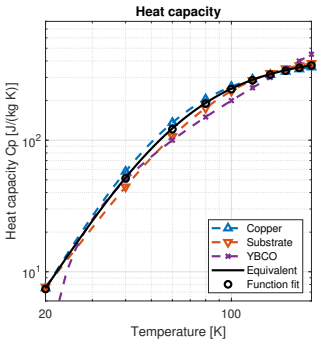

Fig. 19. Specific heat capacity of the individual materials and the equivalent values of the Roebel cable.

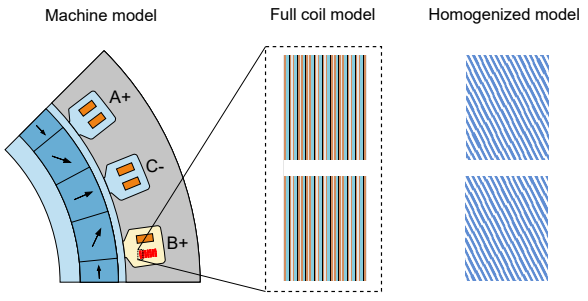

Fig. 20. The modeling approach for the machine analysis (Machine image reproduced with permission from [22]).

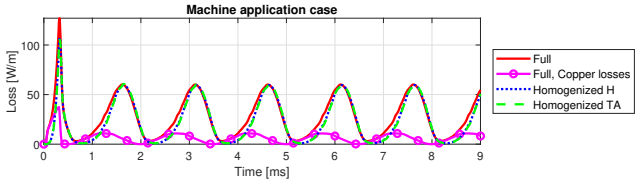

Fig. 21. The electromagnetic losses in the machine case.

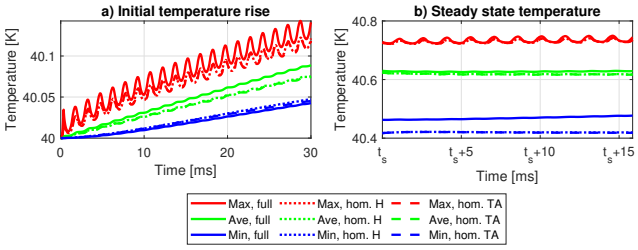

Fig. 22. The a) initial and b) steady-state temperature development for the full and homogenized models for the machine case.

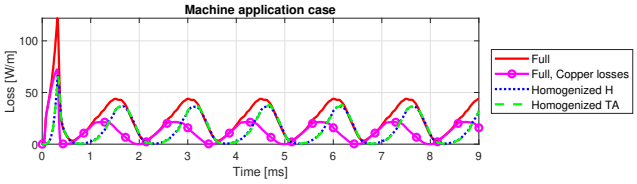

Fig. 23. The electromagnetic losses in the machine case, operating at 25 K.

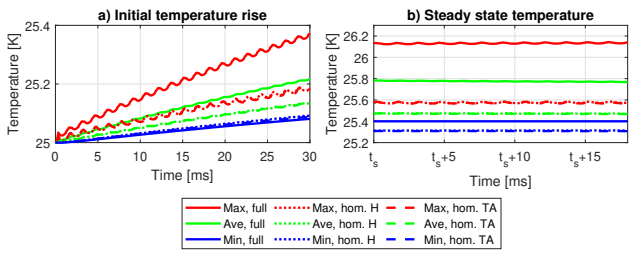

Fig. 24. The a) initial and b) steady-state temperature development for the full and homogenized models for the machine case, operating at 25 K.

which the copper losses are more dominant. An example of such a case occurs when the coils operate at 25 K: the losses in the REBCO layer are reduced due to the increased critical current density, while the lower resistivity of the copper layer leads to larger eddy current losses. The results are shown in Figs. 23 and 24. Now, the copper losses are $40\,\%$ of the total losses, which means the homogenized models significantly underestimate the latter. This leads to an incorrect temperature estimation as well.

V. Discussion

The analyzed cases show that a homogenized HTS coil model with a correct representation of the equivalent thermal properties and correct mesh settings can reproduce the electro-thermal behavior of the coil in a wide range of scenarios.

A. Discussion of Modeling Approach

The equivalent thermal properties of the coil can be calculated by using eqs. (8)-(10). The large difference in thermal conductivity allows for the orthotropic equivalent conductivity to be simplified to

$$k_{eq,w} \approx k_{f,Cu} k_{Cu} \qquad k_{eq,t} \approx k_{ins}/k_{f,ins}, \tag{12}$$

with k_{Cu} and k_{ins} as the thermal conductivity of respectively copper and the insulation material, and $k_{f,X}$ as the volume fraction of material *X*.

The numerical results were found to be strongly dependent on the used mesh and tolerance settings. Three lessons can be drawn to ensure accurate results:

1) The same relative tolerance has been used in all models to compare them, but this occasionally caused spikes in the electromagnetic losses of the homogenized model, visible in Figs. 6 and 10. These spikes did not significantly impact the temperature of the coils. Nonetheless, a lower relative tolerance is recommended when implementing the homogenized model in future analyses.
2) For cases with a perpendicular magnetic field, it is important to have a thin subdomain on the top and bottom of the homogenized coil, as most of the losses are concentrated in this region. These subdomains must be thinner than one HTS tape to ensure accuracy.
3) The accuracy and stability of all models is improved by using a mesh refinement at the edges of the HTS tapes, as shown in Fig. 4.

B. Performance

Overall, the homogenized *T–A*-model shows very similar results to the homogenized H-model presented in [8]. The average losses of both the full and the homogenized models are summarized in Table V. This shows that the homogenized *T–A*-model calculates the losses within an accuracy

TABLE V
Average Electromagnetic Losses and Temperature Rise after 10 Cycles for the Stack and Application Cases

Case	*Full H-model*		*Homogenized H-model*				*Homogenized T–A-model*			
	Q_{tot}	ΔT_{ave}	Q_{tot}	Deviation	ΔT_{ave}	Deviation	Q_{tot}	Deviation	ΔT_{ave}	Deviation
1	27.6 W/m	1.68 K	26.3 W/m	−4.8 %	1.81 K	7.7 %	26.6 W/m	−3.7 %	1.83 K	8.4 %
2	8.3 W/m	0.51 K	8.0 W/m	−2.9 %	0.55 K	8.3 %	8.0 W/m	−3.0 %	0.55 K	8.0 %
3	152.9 W/m	1.75 K	148.1 W/m	−3.2 %	1.91 K	9.5 %	150.3 W/m	−1.7 %	1.91 K	9.5 %
4	9.7 W/m	0.11 K	9.7 W/m	−0.3 %	0.12 K	4.9 %	9.5 W/m	−1.6 %	0.12 K	4.9 %
Machine	27.3 W/m	0.09 K	23.7 W/m	−12.9 %	0.07 K	−14.8 %	23.7 W/m	−13.2 %	0.07 K	−14.9 %

of 5 % over a wide range of scenarios, comparable to the homogenized *H*-model discussed in [8]. In the machine case, the copper losses become relevant, which are not accounted for by the homogenized models. Whether they can be used depends on the operating conditions of the coils, especially their temperature and the magnitude and frequency of the external magnetic fields.

For all stack cases, the temperature development shows that the homogenized model slightly overestimates the temperature rise of the coils, summarized in Table V. This means that the model can be used to give a conservative estimate of the temperature increase due to the transport and magnetization losses. However, in cases where the copper losses become relevant, such as in the machine case, the homogenized model underestimates the total losses and, therefore, the temperature rise. Furthermore, the temperature plots in Section III show that the homogenized model predicts the steady-state temperature of the HTS stacks accurately.

The simulation times for both models are summarized in Table VI. The homogenized *TA*-model shows a further speed improvement over the homogenized *H*-model of approximately a factor 2. Based on these results, and the previous finding in [4] that the performance of homogenized HTS models scale very well for a larger number of tapes, it can be expected that the electro-thermal analysis of HTS coils can be sped up by at least one order of magnitude by using the new homogenized model proposed in this paper.

TABLE VI
SIMULATION TIMES FOR 10 CYCLES FOR THE STACK AND APPLICATION CASES

Case	*Full H-model*	*Homogenized model*		*Speed-up factor*	
		H	*T–A*	*H*	*T–A*
1	23 112 s	2301 s	1267 s	10.0	18.3
2	16 881 s	4511 s	3919 s	3.7	4.3
3	17 152 s	2571 s	1230 s	6.7	13.9
4	17 775 s	4323 s	2220 s	4.1	8.0
Machine	36 002 s	10 943 s	8521 s	3.3	4.2

VI. CONCLUSION

This paper has demonstrated the use of homogenization to simplify and speed up the analysis of the electro-thermal behavior of HTS coils. This was achieved by deriving equivalent orthotropic thermal properties for the coil and coupling this to the existing electromagnetic homogenization method described by Zermeno *et. al.* (2013) [4].

The performance of the new method has been investigated for a range of scenarios. These include transport and magnetization losses, a frequency range between 50 and 300 Hz, and operation at both LN_2 and LH_2 temperatures. Compared to the full model, the losses were reproduced with a difference below 5 %, and the temperature rise and the steady-state temperature distribution agree well. The homogenized model overestimated the temperature increase slightly, which means it can be used as a conservative model to estimate the electro-thermal behavior of the HTS coil. At the same time, the simulation time can be reduced by one order of magnitude compared to the full model, especially if larger coils are analyzed.

The electro-thermal homogenization approach has been demonstrated for both the *H*- and the *T–A*-formulation. The *T–A*-formulation is generally faster, but sometimes suffers from stability issues. Tighter tolerance settings can resolve these issues, but will partly reduce the computational speed improvement. The new homogenization method has also been demonstrated to work for Roebel cables in the analysis of HTS armature windings. It is able to speed up the analysis of HTS machines, and produce accurate results as long as the copper losses are small compared to the HTS losses.

Future work includes extending the application range of the homogenized model to more realistic cases in which the insulation and cooling systems of an electrical machine are modeled as well. This study should also determine in which parameter ranges the copper eddy current losses are significant compared to the HTS losses.

In addition, the accuracy of the results can be improved by using a better model for $J_c(\mathbf{B}, T)$, as the simple model of eqs. (4-5) may not accurately reflect the physical characteristics of the REBCO tapes.

APPENDIX
CURVE FITS OF HOMOGENIZED PROPERTIES

The calculated thermal properties of the homogenized material are fitted to either a logarithmic polynomial, eq. (13), or a logarithmic irrational fraction, eq. (14), similar to what is used in [18].

$$\begin{aligned}\log_{10} y = a + b(\log_{10} T) + c(\log_{10} T)^2 \\ +d(\log_{10} T)^3 + e(\log_{10} T)^4\end{aligned} \tag{13}$$

$$\log_{10} k = \frac{a + cT^{0.5} + eT + gT^{1.5}}{1 + bT^{0.5} + dT + fT^{1.5}} \tag{14}$$

The fitted parameters for the thermal conductivity in the width and thickness direction, as well as the heat capacity, are provided in Table VII for the insulated stacks and the non-insulated Roebel cable.

TABLE VII
FITTED PARAMETERS

	Insulated stack			*Roebel cable*		
	k_w	k_t	C_p	k_w	k_t	C_p
Eq.	(14)	(13)	(13)	(14)	(13)	(13)
a	2.013	-0.9669	5.781	2.594	0.6403	6.552
b	3.823	-2.248	-16.32	1.338	1.036	-21.87
c	8.352	2.89	16.77	3.512	-0.7901	23.45
d	-1.132	-1.122	-6.438	-0.4325	0.2546	-9.372
e	-2.319	0.1428	0.8572	-1.074	-0.02235	1.297
f	0.09708	-	-	0.0383	-	-
g	0.1918	-	-	0.09233	-	-

REFERENCES

[1] Li, C. et al. “Dynamic Resistance of Series-Connected HTS Stacks Considering Electromagnetic and Thermal Coupling”. In: *IEEE Trans. Appl. Supercond.* 32.4 (2022), pp. 1–5.

[2] Ma, J., Geng, J., Chan, W. K., Schwartz, J., and Coombs, T. “A temperature-dependent multilayer model for direct current carrying HTS coated-conductors under perpendicular AC magnetic fields”. In: *Supercond. Sci.Technol.* 33.4 (2020), p. 045007.

[3] Zou, S., Zermeño, V. M. R., and Grilli, F. “Simulation of Stacks of High-Temperature Superconducting Coated Conductors Magnetized by Pulsed Field Magnetization Using Controlled Magnetic Density Distribution Coils”. In: *IEEE Trans. Appl. Supercond.* 26.3 (2016), pp. 1–5.

[4] Zermeno, V. M. R., Abrahamsen, A. B., Mijatovic, N., Jensen, B. B., and Sørensen, M. P. “Calculation of alternating current losses in stacks and coils made of second generation high temperature superconducting tapes for large scale applications”. In: *J. Appl. Phys.* 114.17 (2013), p. 173901.

[5] Berrospe-Juarez, E., Trillaud, F., Zermeño, V. M. R., and Grilli, F. “Advanced electromagnetic modeling of large-scale high-temperature superconductor systems based on H and T-A formulations”. In: *Supercond. Sci.Technol.* 34.4 (2021), p. 044002.

[6] Hu, D. et al. “Influence of the Substrate Layer on the Lightning Current Performance of YBa2Cu3O7-d Tapes”. In: *J. Supercond. Novel Magn.* 30.10 (2017), pp. 2717–2725.

[7] Tomków, L., Mineev, N., Smara, A., Climente-Alarcon, V., and Głowacki, B. A. “Theoretical analysis of heat transport in tilted stacks of HTS tapes at temperatures above 20 K”. In: *Cryogenics* 105 (2020), p. 103017.

[8] Klop, C. L. and Nøland, J. K. “Electro-Thermal Homogenization of High-Temperature Superconductor Stacks”. In: *2023 IEEE Workshop on Power Electronics for Aerospace Applications (PEASA)*. Nottingham, United Kingdom: IEEE, 2023, pp. 1–6.

[9] Benkel, T. et al. “T–A-Formulation to Model Electrical Machines With HTS Coated Conductor Coils”. In: *IEEE Trans. Appl. Supercond.* 30.6 (2020), pp. 1–7.

[10] Shen, B., Grilli, F., and Coombs, T. “Overview of H-Formulation: A Versatile Tool for Modeling Electromagnetics in High-Temperature Superconductor Applications”. In: *IEEE Access* 8 (2020), pp. 100403–100414.

[11] Berrospe-Juarez, E., Zermeño, V. M. R., Trillaud, F., and Grilli, F. “Real-time simulation of large-scale HTS systems: multi-scale and homogeneous models using the T–A formulation”. In: *Supercond. Sci.Technol.* 32.6 (2019), p. 065003.

[12] Sanchez, N. *Cryogenic Properties of Copper*. URL: https://www.copper.org/resources/properties/cryogenic/# (visited on 04/15/2023).

[13] Wimbush, S., Strickland, N., and Pantoja, A. *Critical current characterisation of Shanghai Superconductor Low Field High Temperature 2G HTS superconducting wire. Dataset.* 2022. URL: https://doi.org/10.6084/m9.figshare.19185092.v1 (visited on 04/03/2023).

[14] Kim, Y. B., Hempstead, C. F., and Strnad, A. R. “Critical Persistent Currents in Hard Superconductors”. In: *Phys. Review Lett.* 9.7 (1962), pp. 306–309.

[15] Thakur, K. P., Raj, A., Brandt, E. H., Kvitkovic, J., and Pamidi, S. V. “Frequency-dependent critical current and transport ac loss of superconductor strip and Roebel cable”. In: *Supercond. Sci.Technol.* 24.6 (2011), p. 065024.

[16] Senatore, C., Barth, C., Bonura, M., Kulich, M., and Mondonico, G. “Field and temperature scaling of the critical current density in commercial REBCO coated conductors”. In: *Supercond. Sci.Technol.* 29.1 (2016), p. 014002.

[17] Brambilla, R., Grilli, F., Martini, L., Bocchi, M., and Angeli, G. “A Finite-Element Method Framework for Modeling Rotating Machines With Superconducting Windings”. In: *IEEE Trans. Appl. Supercond.* 28.5 (2018), pp. 1–11.

[18] National Institute of Standard and Technology. *Cryogenics Material Properties*. URL: https : / / trc . nist . gov / cryogenics / materials / materialproperties.htm (visited on 04/03/2023).

[19] Lu, J., Choi, E. S., and Zhou, H. D. “Physical properties of Hastelloy ® C-276™ at cryogenic temperatures”. In: *J. Appl. Phys.* 103.6 (2008), p. 064908.

[20] Själander, M., Jahre, M., Tufte, G., and Reissmann, N. *EPIC: An Energy-Efficient, High-Performance GPGPU Computing Research Infrastructure*. 2022. URL: http://arxiv.org/abs/1912.05848 (visited on 11/23/2023).

[21] Zhang, H. et al. “Modelling of electromagnetic loss in HTS coated conductors over a wide frequency band”. In: *Supercond. Sci.Technol.* 33.2 (2020), p. 025004.

[22] Mellerud, R., Hartmann, C., Klop, C. L., Austad, S., and Nøland, J. K. “Design of a Power-Dense Aviation Motor With a Low-Loss Superconducting Slotted Armature”. In: *IEEE Trans. Appl. Supercond.* 33.8 (2023), pp. 1–13.

[23] Otten, S. “Characterisation of REBCO Roebel cables”. PhD. Karlsruhe: Karlsruhe Institute of Technology, 2019.

[24] Hartmann, C., Mellerud, R., Nøland, J. K., and Nilssen, R. “A Static FEA Framework for Fast Analysis of HTS Armature Windings in AC Superconducting SMPM Machines”. In: *IEEE Trans. Energy Convers.* 38.3 (2023), pp. 2191–2201.

[25] Bagrets, N., Goldacker, W., Schlachter, S. I., Barth, C., and Weiss, K.-P. “Thermal properties of 2G coated conductor cable materials”. In: *Cryogenics* 61 (2014), pp. 8–14.

BIOGRAPHY SECTION

Casper Leonard Klop received the M.Sc. degree in Electrical Engineering from the Technical University of Delft, The Netherlands, in 2022. He is currently pursuing a Ph.D. degree at the Norwegian University of Science and Technology (NTNU) on the topic of cryo-electric propulsion systems for aerospace applications.

Runar Mellerud received his M.Sc. degree in electric power engineering at NTNU in 2021, where he is currently pursuing a Ph.D. degree in superconducting electrical machines for aerospace applications.

Christian Hartmann received the M.Sc. degree in electric power engineering from the Norwegian University of Science and Technology (NTNU), Trondheim, Norway, in 1999. He is a Senior Researcher with the Institute for Energy Technology, and is currently pursuing a Ph.D. degree focusing on cryo-electric propulsion systems for next-generation aviation.

Jonas Kristiansen Nøland (S’14-M’17-SM’22) was born in Drammen, Norway, in 1988. He received the M.Sc. degree in electric power engineering from the Chalmers University of Technology, Gothenburg, Sweden, in 2013, and the Ph.D. degree in engineering physics from Uppsala University, Uppsala, Sweden, in 2017. Since 2018, he has been an Associate Professor with the Department of Electric Power Engineering, Norwegian University of Science and Technology. His current research interests include excitation systems, improved utilization of electrical machines, high-power machinery for aircraft applications, and transportation electrification in general. Dr. Nøland serves as an Associate Editor for the IEEE TRANSACTIONS ON ENERGY CONVERSION, the IEEE TRANSACTIONS ON INDUSTRIAL ELECTRONICS, and the IEEE TRANSACTIONS ON TRANSPORTATION ELECTRIFICATION.